

## Nanobubble Fragmentation and Bubble-Free-Channel Shear Localization in Helium-Irradiated Submicron-Sized Copper

Ming-Shuai Ding,<sup>1</sup> Lin Tian,<sup>1</sup> Wei-Zhong Han,<sup>1,\*</sup> Ju Li,<sup>1,2</sup> Evan Ma,<sup>3</sup> and Zhi-Wei Shan<sup>1,†</sup>

<sup>1</sup>Center for Advancing Materials Performance from the Nanoscale and Hysitron Applied Research Center in China, State Key Laboratory for Mechanical Behavior of Materials, Xi'an Jiaotong University, Xi'an 710049, China

<sup>2</sup>Department of Nuclear Science and Engineering and Department of Materials Science and Engineering, Massachusetts Institute of Technology, Cambridge, Massachusetts 02139, USA

<sup>3</sup>Department of Materials Science and Engineering, Johns Hopkins University, Baltimore, Maryland 21218, USA

(Received 11 July 2016; revised manuscript received 22 August 2016; published 16 November 2016)

Helium bubbles are one of the typical radiation microstructures in metals and alloys, significantly influencing their deformation behavior. However, the dynamic evolution of helium bubbles under straining is less explored so far. Here, by using *in situ* micromechanical testing inside a transmission electron microscope, we discover that the helium bubble not only can coalesce with adjacent bubbles, but also can split into several nanoscale bubbles under tension. Alignment of the splittings along a slip line can create a bubble-free channel, which appears softer, promotes shear localization, and accelerates the failure in the shearing-off mode. Detailed analyses unveil that the unexpected bubble fragmentation is mediated by the combination of dislocation cutting and internal surface diffusion, which is an alternative microdamage mechanism of helium irradiated copper besides the bubble coalescence.

DOI: 10.1103/PhysRevLett.117.215501

Helium bubbles are frequently seen radiation defects produced in metals and alloys that can lead to swelling, hardening, and embrittlement [1–7]. They tend to concentrate along sinks in metals, especially on grain boundaries, thus accelerating the failure of materials by reducing the local bonding area via bubble coalescence [1–7]. In general, helium bubbles in metals have a complex dynamic evolution during service before giving rise to the final catastrophic failure. Therefore, the dynamics of helium bubbles play an important role in determining the mechanical performance of metals. As a result, significant efforts have been made to understand the evolution of helium bubbles under thermal annealing, radiation, or mechanical loading [8–16].

At elevated temperature, helium bubbles tend to develop into faceted polyhedra predicted by Wulff construction, and such faceted bubbles have limited mobility and higher barriers to Ostwald ripening due to the existence of sessile dislocations along the bubble edges [11]. In contrast, under radiation cascade the helium bubbles have high mobility even at room temperature, leading to substantial coarsening and coalescence [10]. Recently, helium bubbles were found to play a combined role of dislocation obstacles and active internal dislocation sources under loading, thus improving the deformation stability of submicron-sized metals [12,14,17]. The nucleation, growth, and coalescence of voids or helium bubbles are regarded as the critical step for causing the final fracture in the 90°-opening mode (the fracture surface is perpendicular to the tensile loading axis) [18,19], and this hypothesis has been recently verified by the *in situ* tensile test of helium-bubbled copper [17]. However, the detailed experimental observation of a single helium bubble under dynamic straining still remains as a

challenge, which therefore limits our basic understanding of the dynamics of helium bubbles in the final stage of failure.

In this work, we developed a new testing sample geometry to facilitate the *in situ* tension of a very thin helium-bubbled copper in order to reveal the dynamics of a single helium bubble. We discover that helium bubbles not only can be severely elongated or coalesced with adjacent bubbles, but also can split into several tiny bubbles under straining. Our finding unveils a critical role of bubble fragmentation in failure of helium-containing copper.

A well-annealed Cu sample was implanted with helium to a fluence of  $2 \times 10^{17}$  ions  $\text{cm}^{-2}$  at 450 °C. Helium bubbles are the sole visible radiation defects remaining and their sizes ranged from 1 to 10 nm with  $\langle D \rangle = 6.6$  nm, and the estimated bubble pressure is less than 1 GPa [17]. The submicron-sized specimens were machined from the main helium-concentrated region (with helium concentration varying from 3 to 8 at.%) by utilizing the focused ion beam method (FIB, FEI Nanolab 600). In order to perform high resolution *in situ* straining, the sample was thinned down to  $\sim 50$  nm in thickness. Thus, the volume-bubble density of such a thin copper sample should be dependent on the position of the cutting, and the different tensile samples have distinct bubble density. Subsequently, the sample was transferred into a transmission electron microscope (TEM, JEOL 2100 F) to conduct *in situ* tension using a Hysitron PicoIndenter 95 (PI95) holder. The shaking of the sample resulting from the unstable mechanical setup (once  $F_{\text{max}} < 50 \mu\text{N}$ ) on a thin sample is the main challenge for high-resolution characterization. In order to avoid such a dilemma, a new push-to-pull sample geometry

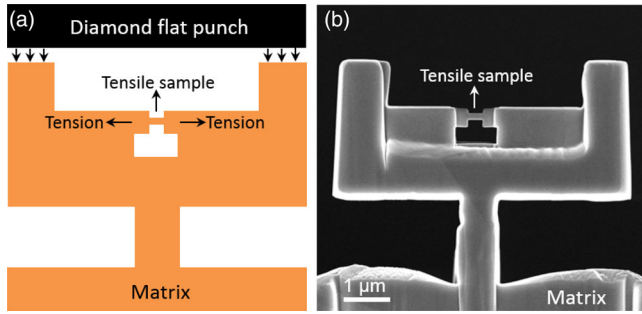


FIG. 1. Schematic illustration of the new push to pull sample geometry. (a) Cartoon of the designed new sample geometry for high resolution observation under *in situ* loading. (b) SEM image of a tensile sample machined by the focused ion beam according to (a).

was designed to stabilize the mechanical response for an ultrathin tensile sample [Fig. 1(a)]. When pushing the convex pillars at the two ends [Fig. 1(a)], an approximately uniaxial tensile strain will be generated on the middle tiny tensile sample. In this case, the applied force is large enough ( $F_{\min} > 200 \mu\text{N}$ ) to stabilize the overall testing system and therefore eliminate the usual sample shaking. The loading rate was set to be 1–5 nm/s, corresponding to a strain rate of  $4 \times 10^{-3}$  to  $2 \times 10^{-2}$ /s. The deformation processes were recorded by a charge-coupled device camera (Gatan 833 CCD) with capture rate of 10 frames/s.

Figure 2 shows an example of significant elongation of helium bubbles under tensile deformation. The sample was first loaded into the plastic deformation regime (with some necking) and then unloaded, as displayed in Fig. 2(a). At this point, most of the helium bubbles are still nearly spherical, as highlighted by the bubbles labeled as b1 to b5. With reloading the sample to an average strain of 1.24, these bubbles evolved from initial spherical into a rodlike elongated shape, especially for the bubbles located in the middle region, as shown in Fig. 2(b). The significant shape evolution of b3 is highlighted by the cartoons in Figs. 2(a) and 2(b). The extent of elongation of bubbles can be quantified by the variation of aspect ratio during straining, as shown by the inset in Fig. 2(b). In general, the aspect ratio of bubbles increases with increasing strain. For the same strain level, it increases from the edge to the center of the necking zone (b1 to b3). The aspect ratio of b3 reaches as high as 8 at an average strain of 1.24, corresponding to a width reduction from 10.3 to 4.5 nm, showing the local superdeformability of a single helium bubble. The slight asymmetry of elongated bubbles is likely due to the heterogeneous strain distribution.

The width of the bubble will continue to decrease with the increasing strain. We then found that, once a critical value of the bubble width has been reached, such as  $\sim 1$  nm, the helium bubble splits into several nanoscale bubbles. This will be referred to hereafter as helium bubble fragmentation. Figure 3 displays a helium-bubbled copper sample loaded along  $[5\ 1\ \bar{2}1]$ . Once necking started, some

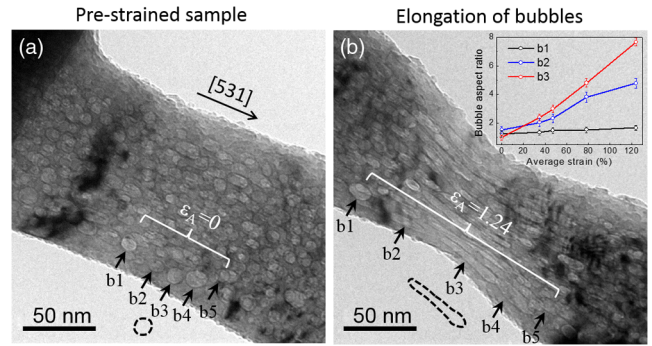


FIG. 2. Local plastic strain-induced elongating of helium bubbles. (a) Some bubbles were slightly elongated once necking deformation started, and marked as  $\varepsilon_A = 0$ . (b) Severely elongated bubbles in the middle of the sample when  $\varepsilon_A = 1.24$ . The inset in (b) is the plot of the aspect ratio of the tracked bubbles versus the average strain. The strain was determined according to the relative positions of b1 to b5.

of the bubbles were severely elongated, as the one labeled by black dashed contour in Fig. 3(a), with an aspect ratio of 3.67 and a width of 3 to 4 nm. With further tensile deformation, the left part of the bubble was rapidly narrowed down from 4 nm in width to  $\sim 1$  nm, and evolved into a long rodlike bubble (highlighted by black bracket), while the right part only slightly elongated due to inhomogeneous local strain [Fig. 3(b)]. The state of the bubble in Fig. 3(b) likely reached a critical point: further deformation split the long rodlike bubble into three segments, as

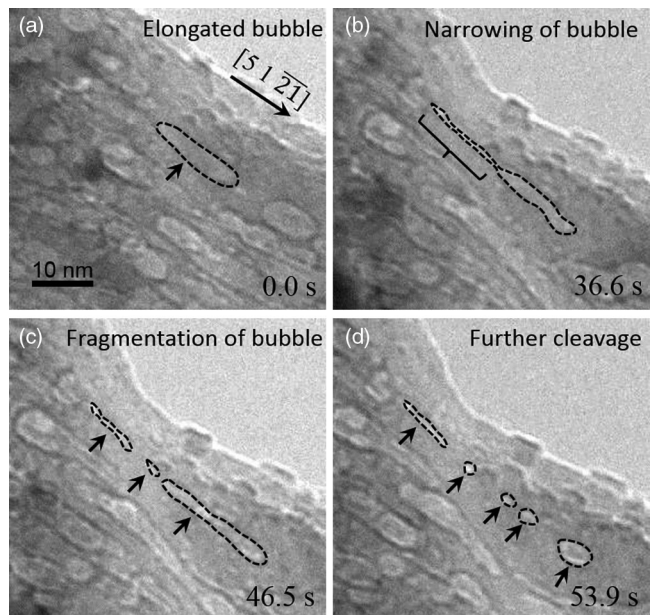


FIG. 3. Fragmentation of a helium bubble into several tiny bubbles during severe straining. (a) Slightly elongated bubbles after stretch. (b) Left part of the bubble shrunk down to  $\sim 1$  nm in width with further deformation. (c) The severely elongated bubble fragmented into three segments. (d) Further fragmentation of the stretched bubbles into five tiny bubbles.

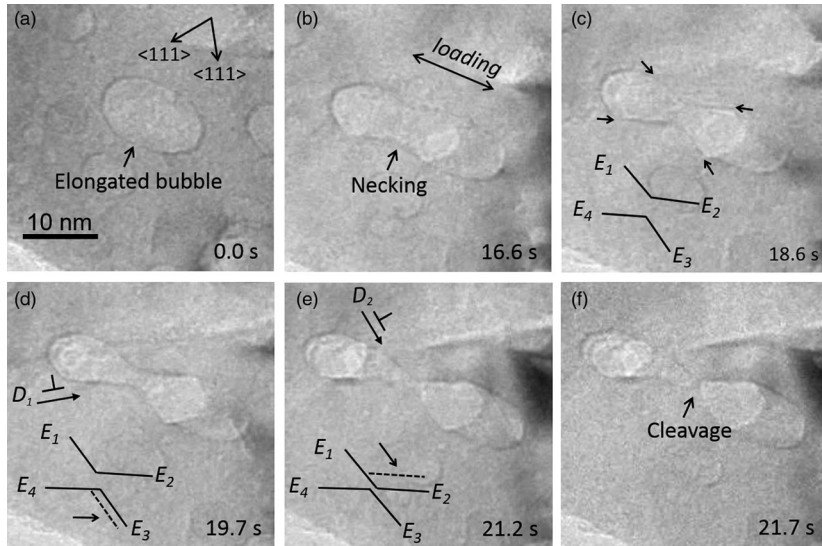


FIG. 4. Dislocation slip-induced helium-bubble necking and cleavage. (a) Slightly elongated bubble, (b) Bubble starts to neck. (c) Dislocation slip leads to the formation of four flat edges in the bubble necking region, and labeled as  $E_1$ ,  $E_2$ ,  $E_3$ , and  $E_4$ , respectively. (d) Further dislocation slip results in the movement of  $E_3$  towards the right side. (e) Further dislocation slip results in the movement of  $E_2$  towards the down part, and finally the space between  $E_1$  and  $E_3$  is reduced. (f) Final cleavage of the bubble once the local width is narrower than 1 nm.

marked by the black arrows in Fig. 3(c). This is likely the first experimental observation of the helium bubble fragmentation under deformation (details in the Supplemental Material, movie S1 [23]). In the subsequent straining, deformation was localized in the right section of the helium bubble in Fig. 3(c), and led to severe reduction of bubble width and, finally, splitting into three parts [Fig. 3(d)]. Our *in situ* studies confirm that the severe plastic straining can cause significant reduction of bubble width. Once a critical width of  $\sim 1$  nm was reached, like just a few vacancies across, the bubble would fragment in a fashion like nanowires at the elevated temperature [20,21]. While the coalescence of helium bubbles at the final stage of failure is expected [22], the fragmentation of the helium bubble is quite unexpected.

Besides the extreme elongation induced fragmentation of helium bubble, the dislocation cutting caused bubble cleavage was also observed during the *in situ* tensile test. Figure 4 displays a typical dislocation slip-induced necking and subsequent fragmentation process of a helium bubble. During tension, helium bubbles have undergone a different degree of the elongation, as shown in Fig. 4(a). With further loading, the bubble in the middle was stretched into a dumbbell shape with local necking, as displayed in Fig. 4(b). Four flat edges were gradually formed in the necked part of the bubble, as marked in Fig. 4(c) as  $E_1$ ,  $E_2$ ,  $E_3$ , and  $E_4$ , respectively. These edges are formed nearly along the two slip planes of helium-bubbled copper. The four edges were contoured and placed at the left-bottom corner in order to illustrate their evolution during further straining. As the tension proceeds, we first find that  $E_3$  moves toward right due to the dislocation slip along the  $D_1$  slip system, as indicated in Fig. 4(d). Then, dislocation slip along the  $D_2$  slip system brings  $E_2$  down. This reduces the spacing between  $E_1$  and  $E_3$  to the critical value of  $\sim 1$  nm, as shown in Fig. 4(e) and movie S2 in [23]. Finally, the bubble “fractured” in the necked region, splitting into two bubbles. The tips are sharp just after splitting and then shrink rapidly to reach a smooth

surface after 0.2 s, suggesting shape recovery driven by local internal surface diffusion, as shown in movie S2 of the Supplemental Material [23]. In general, the fragmentation of helium bubbles is a common phenomenon appearing in all of the 15 tests performed, and the typical examples are displayed in Figs. 3 and 4, and S1 of [23].

Our *in situ* studies indicated that both the dislocation slip and internal surface diffusion play important roles in the fragmentation dynamics of helium bubbles. Figure 5(a) is a schematic illustration of the fragmentation mechanism of helium bubbles under severe plastic deformation. During the straining, equilibrium helium bubbles can be sheared by dislocations [17]. A surface step with the magnitude of the Burgers vector can be formed after one dislocation cutting, as illustrated in Fig. 5(a). In order to minimize the energy of a sharp slip step of several Burgers vectors on the bubble surface, local internal surface diffusion driven by surface tension and bubble pressure will be activated to smoothen the slip step [22,24], and finally a curved surface is formed [Fig. 5(a)]. Helium bubble necking or homogeneous elongation can take place after multiple dislocation cuttings with the assistance of internal surface diffusion, as illustrated in Fig. 5(a).

When the local width of the bubble in the necking zone is less than 1 nm, the fragmentation of the bubble happens rapidly, resulting in the formation of two separate bubbles with sharp tips. These bubble tips are quite unstable owing to local high curvature or surface tension [24], and with the assistance of local internal surface diffusion, the sharp tips quickly shrink to form a smooth surface [Fig. 5(a)]. According to the local curvature driven surface diffusion [25],

$$D_s \sim \frac{h_0 R_0^3 k_B T}{t \gamma \Omega \delta_s}, \quad (1)$$

where  $D_s$  is the bubble internal surface diffusivity,  $h_0 \approx 2 \sim 3$  nm is the height of the bubble sharp tip,  $R_0 = 0.5$  nm is the radius of bubble tip,  $t = 0.2$  s is the time to evolve from the sharp tip to the smooth surface,

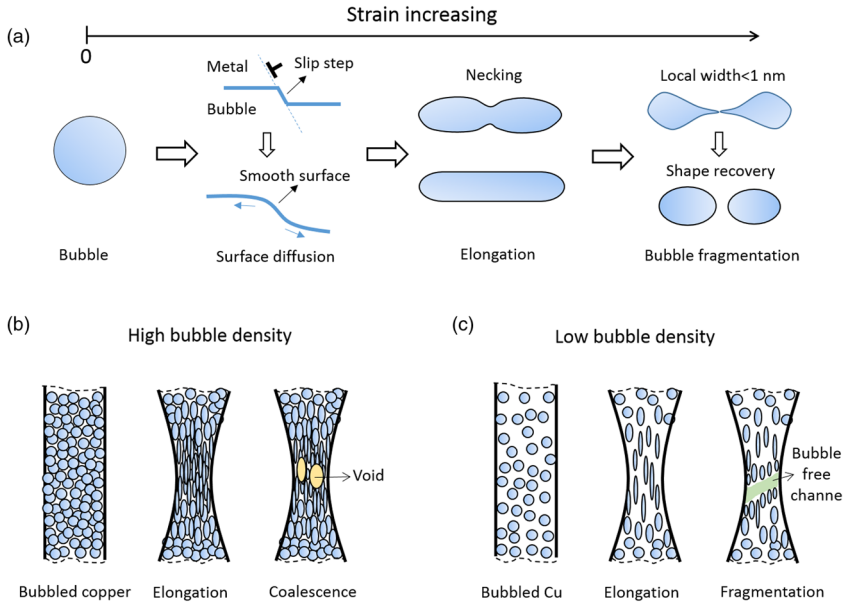


FIG. 5. Dislocations cutting and internal surface diffusion mediated bubble elongation, necking, and cleavage result in different fracture models. (a) Dislocation-bubble interaction and internal surface diffusion-induced bubble fragmentation. (b) Copper sample with high bubble density tends to fail via bubble coalescence. (c) Copper sample with low bubble density prone to shear localization along bubble-free channel formed via bubble fragmentation. However, bubble coalescence and fragmentation could occur simultaneously in a single test, which depends on the local bubble spacing. The influence of bubble density on the bubble coalescence or fragmentation is established based on information from the multiple *in situ* tensile tests.

$\gamma = 2.0 \text{ J m}^{-2}$  is the surface energy,  $\delta_s = 0.3 \text{ nm}$  is the surface layer thickness,  $k_B$  is the Boltzmann constant,  $T$  is the temperature, and  $\Omega$  is the atomic volume. Based on Eq. (1), the sharper the bubble tip or step just after fragmentation, the faster the bubble recovers back to spherical shape. A typical value of  $D_s = 7.3 \times 10^{-19} \text{ m}^2/\text{s}$  was estimated from the *in situ* experimental data. This estimate has the same magnitude with the prediction from the empirical rule of surface diffusivity of bulk metals [26],

$$D_s = 0.014 \exp\left(-\frac{6.54T_m}{T}\right) \text{ cm}^2 \text{ s}^{-1}, \quad (2)$$

where  $T_m$  is the melting temperature of Cu. The calculated  $D_s$  is  $1.96 \times 10^{-19} \text{ m}^2/\text{s}$  for Cu at room temperature. The slightly larger surface diffusivity measured from the *in situ* experiment than the calculated value from Eq. (2) is likely due to the size effect on melting temperature of Cu nanoligaments and the bubble pressure driven shape recovery, both of which will promote local surface diffusion [22,27]. As for the fragmentation, there are two possible driving forces. One is that a train of dislocations cutting the bubble directly bring the upper surface to within  $\sim 1 \text{ nm}$  of the lower one, and this mechanism is likely dominant during the plastic straining (Fig. 4). Another is Rayleigh instability controlled morphological evolution once the aspect ratio of a cylindrical bubble reaches a critical value, driven by the reduction of surface energy. A pure fragmentation of helium bubble controlled by Rayleigh instability is demonstrated in Fig. S2. After aging in vacuum for 11 min, the elongated bubble in Fig. S2 fragmented into two parts, quite similar to the fragmentation behavior of nanowires at elevated temperature [20,21]. The coalescence of helium bubbles was also observed, which is likely a reverse process of bubble fragmentation, as shown in Fig. S3.

Interestingly, the current study found that the fragmentation of helium bubbles can be an alternative microdamage

mechanism beside bubble coalescence. Figure S4 shows an example of the final fracture of a helium-bubbled copper sample, in which a bubble-free channel was formed due to the bubble fragmentation, similar to the dislocation-free channel generated by dislocation–radiation-defect interactions [28–31]. The role of the bubble-free channel is similar to the defect-free channels observed in irradiated metals [28–31], which will facilitate shear localization and accelerate the failure. In such  $\sim 45^\circ$  shearing-off mode, the locations of the split events of multiple bubbles happen to be aligned along a crystallographic slip line direction, which removes the obstacles (the bubbles) so that a certain kind of dislocation can glide and multiply very rapidly in a very narrow band. Furthermore, the copper samples with high-bubble density tend to failure via bubble coalescence, while the samples with low-bubble density are prone to shear localization along the bubble-free channel formed via bubble fragmentation. However, bubble coalescence and fragmentation could occur simultaneously in a single test, which depends on the local bubble spacing. The current finding suggests that the microdamage processes of helium-bubbled copper can be divided into four stages, including bubble-dislocation interaction, bubble elongation, bubble coalescence or fragmentation, and final fracture, as illustrated in Figs. 5(b) and 5(c).

In summary, by employing the *in situ* micromechanical testing combined with the new design of the tensile sample geometry, we have successfully captured the details of the dynamic evolution of helium bubbles under plastic flow. The underlying mechanisms of the bubble elongation, necking and fragmentation, or coalescence are mediated by dislocation slip and local internal surface diffusion. Notably, the bubble fragmentation is the critical step to produce a bubble-free channel, which is an alternative microdamage mechanism of helium-bubbled copper. Our findings shed new light on the understanding of the

dynamic evolution of helium bubbles under straining and the failure mechanism of helium-irradiated metals.

This work was supported by the NSFC (No. 51471128, No. 51231005, No. 51321003). W. Z. H. acknowledges the support of Youth Thousand Talents Program of China and the Young Talent Support Plan of XJTU. J. L. acknowledges supports by NSF Grant No. DMR-1410636. W. Z. H. appreciates the assistance of Engang Fu and Yongqiang Wang in ion implantation.

\*wzhanxjtu@mail.xjtu.edu.cn

†zwshan@mail.xjtu.edu.cn

- [1] D. Kramer, H. R. Brager, C. G. Rhodes, and A. G. Pard, Helium embrittlement in 304 stainless steel, *J. Nucl. Mater.* **25**, 121 (1968).
- [2] H. Trinkaus and H. Ullmaier, High temperature embrittlement of metals due to helium: is the lifetime dominated by cavity growth or crack growth?, *J. Nucl. Mater.* **212**, 303 (1994).
- [3] H. Trinkaus and B. Singh, Helium accumulation in metals during irradiation—where do we stand?, *J. Nucl. Mater.* **323**, 229 (2003).
- [4] P. Jung, J. Henry, and J. Chen, Tensile properties of candidate structural materials for high power spallation sources at high helium contents, *J. Nucl. Mater.* **343**, 275 (2005).
- [5] J. Henry, L. Vincent, X. Averty, B. Marini, and P. Jung, Effect of a high helium content on the flow and fracture properties of a 9Cr martensitic steel, *J. Nucl. Mater.* **367**, 411 (2007).
- [6] G. R. Odette, M. J. Alinger, and B. D. Wirth, Recent developments in irradiation-resistant steels, *Annu. Rev. Mater. Res.* **38**, 471 (2008).
- [7] W. Z. Han, M. J. Demkowicz, N. A. Mara, E. G. Fu, S. Sinha, A. D. Rollett, Y. Q. Wang, J. S. Carpenter, I. J. Beyerlein, and A. Misra, Design of irradiation tolerant materials via interface engineering, *Adv. Mater.* **25**, 6975 (2013).
- [8] C. DeW, Van Siclen, R. N. Wright, and S. G. Usmar, Anomalous helium bubble diffusion in dilute aluminum alloys, *Phys. Rev. Lett.* **68**, 3892 (1992).
- [9] M. Miyamoto, K. Ono, K. Arakawa, and R. C. Birtcher, Effects of cascade damages on the dynamical behavior of helium bubbles in Cu, *J. Nucl. Mater.* **367**, 350 (2007).
- [10] Q. Wei, N. Li, K. Sun, and L. M. Wang, The shape of bubbles in He-implanted Cu and Au, *Scr. Mater.* **63**, 430 (2010).
- [11] N. Li, N. Mara, Y. Wang, M. Nastasi, and A. Misra, Compressive flow behavior of Cu thin films and Cu/Nb multilayers containing nanometer-scale helium bubbles, *Scr. Mater.* **64**, 974 (2011).
- [12] Y. Fan, A. Kushima, S. Yip, and B. Yildiz, Mechanism of void nucleation and growth in bcc Fe: Atomistic simulations at experimental time scales, *Phys. Rev. Lett.* **106**, 125501 (2011).
- [13] W. Z. Han, M. J. Demkowicz, E. G. Fu, Y. Q. Wang, and A. Misra, Effect of grain boundary character on sink efficiency, *Acta Mater.* **60**, 6341 (2012).
- [14] Q. Guo, P. Landau, P. Hosemann, Y. Q. Wang, and J. R. Greer, Helium implantation effects on the compressive response of Cu nanopillars, *Small* **9**, 691 (2013).
- [15] L. Sandoval, D. Perez, B. P. Uberuaga, and A. F. Voter, Competing kinetics and helium bubble morphology in W, *Phys. Rev. Lett.* **114**, 105502 (2015).
- [16] A. Reichardt, M. Lonescu, J. Davis, L. Edwards, R. P. Harrison, P. Hosemann, and D. Bhattacharyya, In situ micro tensile testing of He + 2 ion irradiated and implanted single crystal nickel film, *Acta Mater.* **100**, 147 (2015).
- [17] M. S. Ding, J. P. Du, L. Wan, S. Ogata, L. Tian, E. Ma, W. Z. Han, J. Li, and Z. W. Shan, Radiation-induced helium nanobubbles enhance ductility in submicron-sized single-crystalline copper, *Nano Lett.* **16**, 4118 (2016).
- [18] M. Meyers and K. Chawla, *Mechanical Behavior of Materials*, 2nd ed. (Cambridge University Press, Cambridge, England, 2009), p. 474.
- [19] T. L. Anderson, *Fracture Mechanics: Fundamentals and Applications*, 3rd ed. (Taylor and Francis Group, London, 2005), p. 219.
- [20] C. Brechignac, Ph. Cahuzac, F. Carlier, C. Colliex, J. Leroux, A. Masson, B. Yoon, and U. Landman, Instability driven fragmentation of nanoscale fractal islands, *Phys. Rev. Lett.* **88**, 196103 (2002).
- [21] M. E. Toimil Molares, A. G. Balogh, T. W. Cornelius, R. Neumann, and C. Trautmann, Fragmentation of nanowires driven by Rayleigh instability, *Appl. Phys. Lett.* **85**, 5337 (2004).
- [22] G. S. Was, *Fundamentals of Radiation Materials Science* (Springer, New York, 2007), p. 700.
- [23] [23] See Supplemental Material at <http://link.aps.org/supplemental/10.1103/PhysRevLett.117.215501> for supplemental figures and movies.
- [24] P. Shewmon, *Diffusion in Solids*, 2nd ed. (The Minerals, Metals & Materials Society, Pittsburgh, PA, 1989), p. 208.
- [25] L. Tian, J. Li, J. Sun, E. Ma, and Z. W. Shan, Visualizing size-dependent deformation mechanism transition in Sn, *Sci. Rep.* **3**, 2241 (2013).
- [26] K. N. Tu, *Solder Joint Technology*, Springer Series in Materials Science, (Springer, New York, 2007), p. 211.
- [27] G. Guisbiers, M. Kazan, O. Van Overschelde, M. Wautelet, and S. Pereira, Mechanical and thermal properties of metallic and semiconductive nanostructures, *J. Phys. Chem. C* **112**, 4097 (2008).
- [28] Y. Dai and M. Victoria, Defect cluster structure and tensile properties of Cu single crystals irradiated with 600 MeV protons, *MRS Symp. Proc.* **439**, 319 (1997).
- [29] T. D. de la Rubia, H. M. Zbib, T. A. Khraishi, B. D. Wirth, M. Victoria, and M. J. Caturla, Multiscale modelling of plastic flow localization in irradiated materials, *Nature (London)* **406**, 871 (2000).
- [30] Y. Fan, Y. N. Osetskiy, S. Yip, and B. Yildiz, Mapping strain rate dependence of dislocation-defect interactions by atomistic simulations, *Proc. Natl. Acad. Sci. U.S.A.* **110**, 17756 (2013).
- [31] D. C. Johnson, B. Kuhr, D. Farkas, and G. S. Was, Quantitative analysis of localized stresses in irradiated stainless steels using high resolution electron backscatter diffraction and molecular dynamics modeling, *Scr. Mater.* **116**, 87 (2016).